Dimensional crossover in the carrier mobility of two-dimensional semiconductors: the case of InSe

Wenbin Li, Samuel Poncé, and Feliciano Giustino*

Department of Materials, University of Oxford, Parks Road, Oxford, OX1 3PH, United Kingdom

E-mail: feliciano.giustino@materials.ox.ac.uk

Phone: +44 1865 612790

Abstract

Two-dimensional (2D) semiconductors are at the center of an intense research effort aimed at developing the next generation of flexible, transparent, and energy-efficient electronics. In these applications the carrier mobility, that is the ability of electrons and holes to move rapidly in response to an external voltage, is a critical design parameter. Here we show that the interlayer coupling between electronic wavefunctions in 2D semiconductors can be used to drastically alter carrier mobility and dynamics. We demonstrate this concept by performing state-of-the-art *ab initio* calculations for InSe, a prototypical 2D semiconductor that is attracting considerable attention owing to its exceptionally high electron mobility. We show that the electron mobility of InSe can be increased from 100 to 1000 $cm^2V^{-1}s^{-1}$ by exploiting the dimensional crossover of the electronic density of states from 2D to 3D. By generalizing our results to the broader class of layered materials, we discover that dimensionality plays a universal role in the transport properties of 2D semiconductors.

Key words: Indium selenide, carrier mobility, electron-phonon interactions, two-dimensional materials, interlayer interaction, dimensional crossover

Owing to their extraordinary optoelectronic properties, 2D materials have become a focal point of research in nanoelectronics and nanophotonics for the post-Moore Era.[1–5] Among the properties of 2D materials that are essential to the operation of transistors and light-emitting diodes, the carrier mobility occupies a special place, because it underpins fundamental performance metrics such as switching frequency and power consumption. In order to realize high-mobility transistors, it is paramount to understand the microscopic mechanisms underlying carrier mobilities in 2D materials and how to control them.

Recently, 2D InSe has emerged as a prime candidate for post-silicon electronics.[6] Indeed, room-temperature electron mobilities as high as 1000 $cm^2V^{-1}s^{-1}$ have been reported.[6–8] This value is much higher than in other gapped 2D semiconductors like MoS_2,[9] and is comparable to that of black phosphorous, with the added advantage that InSe exhibits superior environmental stability.[6] Intriguingly, the electron mobility of InSe appears to increase from a trilayer sample to a six-layer sample, while data for the monolayer have not been reported yet.[6] These findings raise the question on what mobility one should expect for the monolayer, and what is the role of dimensionality in the carrier mobility of 2D materials.

In this work we show that the measured layer-dependence of the electron mobility in InSe and in other semiconductors such as MoS_2[10,11] is a novel, intrinsic, and universal mechanism related to the dimensional crossover of the electronic structure from 2D to 3D. In order to illustrate this point, we begin by investigating the atomistic origin of carrier mobilities and their layer dependence in InSe as a representative example, and then we generalize our findings to a broader class of 2D materials by developing a tight-binding model that captures the essential physics.

InSe is a chalcogenide semiconductor that can be exfoliated into individual layers.[6] Each layer consists of four atomic planes, two inner In planes and two outer Se planes, with the atoms arranged in an hexagonal lattice (Figure 1*A*). In bulk InSe the individual layers are separated by approximately 8 Å, and are held together by van der Waals forces. Bulk InSe can exist in several polytypes, which differ by their stacking geometry, with the β and γ

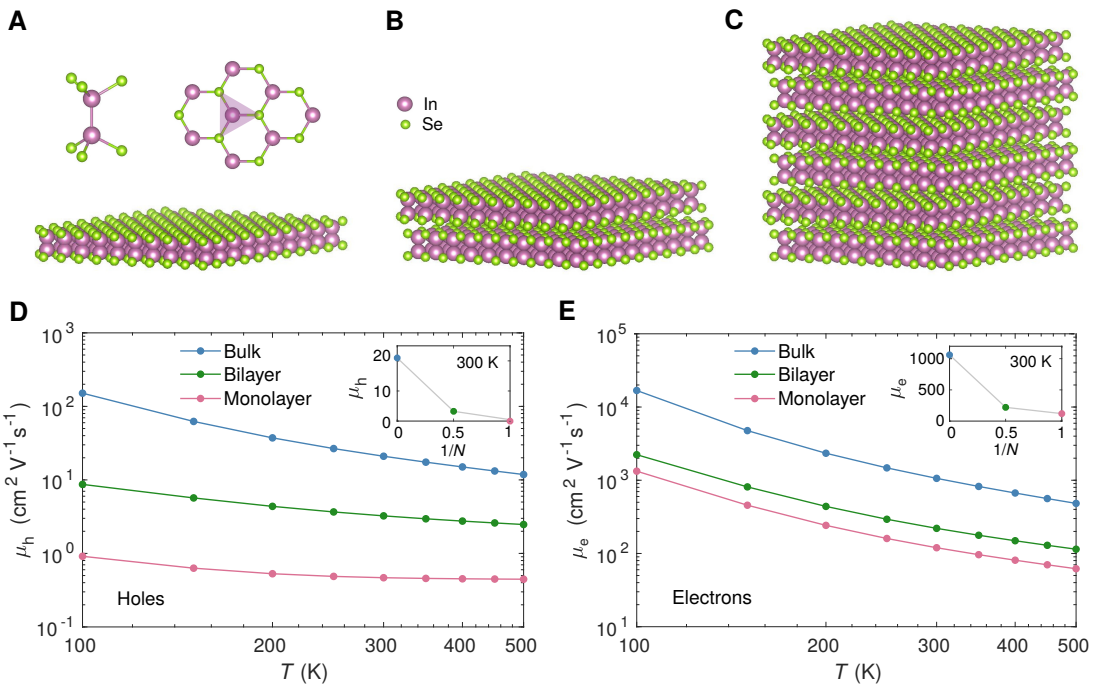

Figure 1: **Atomistic models and *ab initio* carrier mobilities of InSe.** (**A**–**C**) Schematic representations of monolayer, bilayer, and bulk InSe, respectively. In (**A**) we also show the side and top views of the basic trigonal-prismatic unit of monolayer InSe, in a ball-stick model. (**D** and **E**) Temperature-dependent in-plane hole mobilities and electron mobilities of monolayer, bilayer, and bulk InSe. The calculations are performed using the *ab initio* Boltzmann transport equation, as described in the Methods. The insets show the calculated room-temperature mobilities vs. the reciprocal of the number of layers, $1/N$, for $N = 1, 2, \infty$.

phases being the most commonly reported.[12–14] The atomistic representations of monolayer, bilayer, and bulk InSe are illustrated in Figure 1*A*–*C*, while the different polytypes are shown in Supplementary Figure S1*A* and S1*B*. Despite the different stacking sequence, we find that the electronic structure and transport properties of the two polytypes are very similar (Supplementary Figure S1 and S2), therefore we focus on the β phase for definiteness.

We calculate the *intrinsic*, phonon-limited carrier mobility of monolayer, bilayer and bulk InSe using the state-of-the-art *ab initio* Boltzmann transport formalism[15] (see Methods). The calculated in-plane electron and hole mobilities are shown in Figure 1*D* and *E*. We can see that the mobilities decrease upon increasing temperature. This is expected since we are considering only electron-phonon scattering processes. Furthermore, the electron mobility is

Table 1: **Carrier mobilities and effective mass of monolayer, bilayer, and bulk InSe.** Comparison between the calculated in-plane electron and hole mobilities and effective masses of InSe at 300 K, as a function of the number of layers. In the case of holes in monolayer and bilayer InSe, we report the 2D harmonic average of the anisotropic effective mass tensor. Our calculations are in good agreement with available experimental data, as shown in Table S1.[6,17–19]

	Mobility ($cm^2V^{-1}s^{-1}$)		Effective mass (m^*/m_e)	
	Electron	Hole	Electron	Hole
Monolayer	120	0.5	0.16	3.4
Bilayer	220	3	0.14	1.6
Bulk	1060	21	0.10	2.6

two orders of magnitude higher than the hole mobility. Most importantly, both the electron and hole mobilities are very sensitive to the number of layers (insets of Figure 1*D* and *E*). For example, at 300 K the electron mobility decreases from 1060 $cm^2V^{-1}s^{-1}$ in the bulk to 220 and 120 $cm^2V^{-1}s^{-1}$ in the bilayer and monolayer, respectively. Similarly, the hole mobility decreases from 21 to 3 to 0.5 $cm^2V^{-1}s^{-1}$ from bulk to bilayer to monolayer.

While the results shown in Figure 1 are calculated entirely from first principles, it is illuminating to rationalize these data using the elementary Drude model.[16] In this model the mobility μ of a carrier is related to its effective mass m^* and lifetime τ via $\mu = e\tau/m^*$, where e is the electron charge. In order to check whether the trends seen in Figure 1 may be explained by the effective masses, in Table 1 we report the calculated band masses for monolayer, bilayer, and bulk InSe, and compare with the corresponding room-temperature mobilities. From this table we see that the increase in mobility from monolayer to bulk and from holes to electrons are much more pronounced (between one and two orders of magnitude) that the corresponding decrease in the effective masses. Therefore the differences in the band masses cannot account for the trends seen in Figure 1, and we must direct our attention to the other parameter appearing in the Drude model, the carrier lifetime.

In Figure 2*A* and *B* we compare the reciprocal of the carrier lifetimes, or scattering rates,

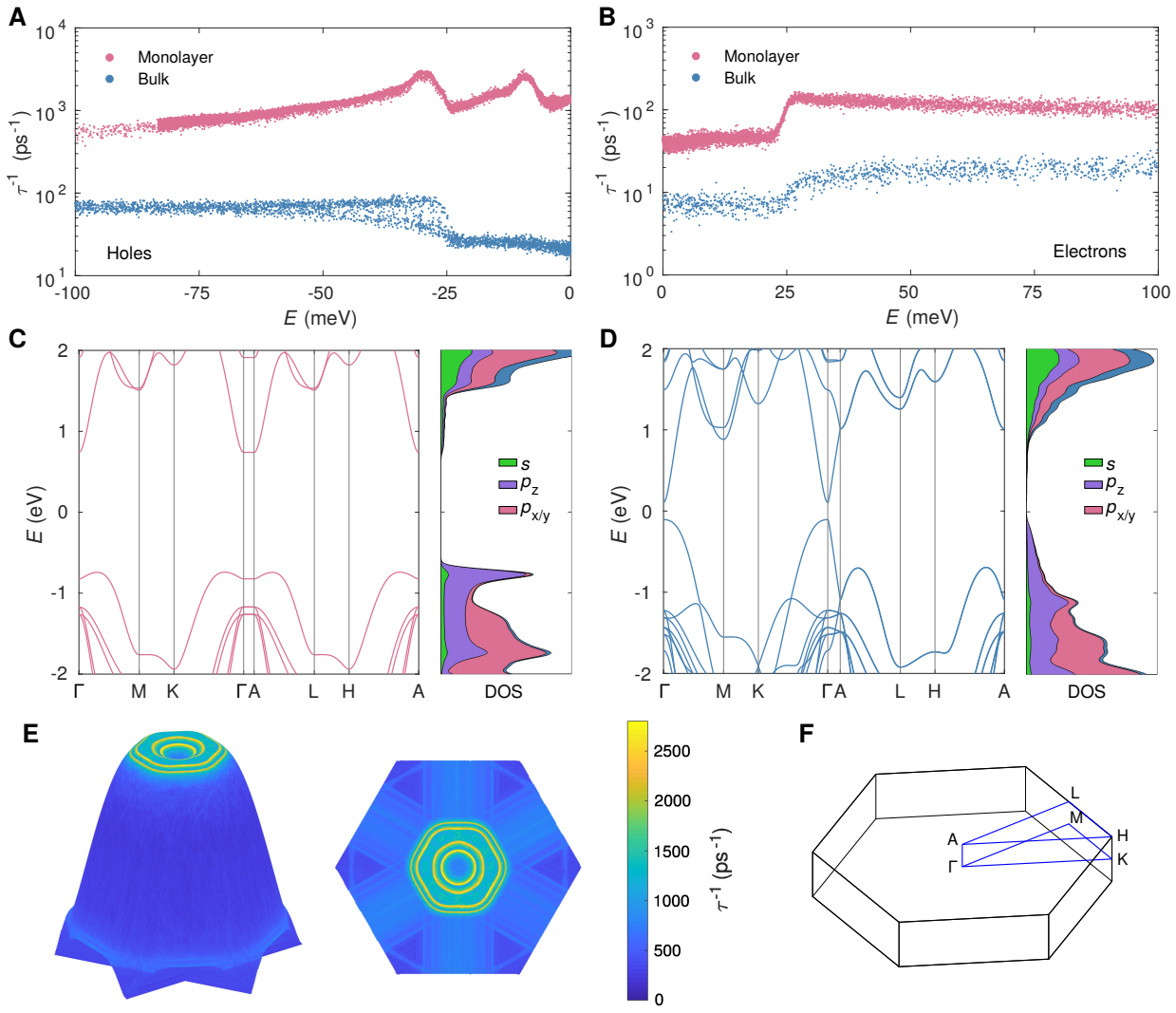

Figure 2: **Carrier scattering rates of monolayer and bulk InSe.** (**A** and **B**) Hole (left) and electron (right) scattering rate of monolayer InSe and bulk, at 300 K. Energies are given with respect to the valence and conduction band edge, respectively. (**C** and **D**) Electronic band structures of monolayer (left) and bulk (right) InSe, calculated using density functional theory (DFT) along the reciprocal space path shown in (**F**). The corresponding density of states (DOS) and its decomposition into atomic-orbital contributions are shown alongside. The s, p_z, and p_x/p_y orbitals are from both In and Se atoms. (**E**) Side and top views of the 2D scattering rates of hole carriers in monolayer InSe. The rates are color-coded on the band structure.

$1/\tau$, in monolayer and bulk InSe, for energies within 100 meV from the band edges. The scattering rates of bilayer InSe are shown in Supplementary Figure S3. Here we see that the scattering rates in the monolayer are approximately one order of magnitude higher than in the bulk, and that holes have scattering rates one order of magnitude higher than electrons.

These observations are consistent with the calculated carrier mobilities in Table 1, and indicate that the trends seen in Figure 1 originate primarily from differences in the carrier lifetimes.

Within time-dependent perturbation theory, the lifetimes can be obtained from Fermi golden's rule;[20] in the simplest approximation they are proportional to the strength of the electron-phonon coupling, $|g|^2$, and to the density $D(E)$ of final electronic states available for scattering at the energy E, $1/\tau \propto |g|^2 D(E)$ (see Methods). Let us analyze each term separately.

To investigate the impact of the electron-phonon coupling $|g|^2$, in Supplementary Figure S4 we break down the scattering rates into contributions from each phonon mode. From this decomposition we see that, at variance with earlier assumptions,[17,21] the scattering rates of electron carriers are dominated by the coupling to longitudinal-optical (LO) phonons, i.e. the Fröhlich interaction. This is particularly evident from the abrupt increase of the scattering rates at electron energies above 26 meV, i.e. above the threshold for the emission of LO phonons (Figure 2*B* and Supplementary Figure S5). How does this Fröhlich interaction depend on the number of layers? In Supplementary Figure S6 we compare the strength of this coupling in the monolayer and in the bulk, and we find that the results are essentially identical. This means that the electron-phonon matrix elements $|g|^2$ cannot account for the thickness dependent electron lifetimes seen in Figure 2*B*. In the case of hole carriers, the dominant scattering mechanism in bulk InSe is also Fröhlich coupling (Supplementary Figure S4*C*), and for long-wavelength phonons the matrix elements $|g|^2$ are the same as for electron carriers.[22] On the other hand, in the monolayer, hole carriers experience an additional scattering mechanism, originating from coupling to longitudinal-acoustic (LA) phonons (Supplementary Figure S4*D*). This new mechanism is responsible for the additional peak in the hole carrier scattering rate of monolayer InSe at an energy around 9 meV in Figure 2*A*, and is connected with the warped nature of the valence band top in monolayer InSe,[23,24] as illustrated in Figure 2*C* and *E*. The corresponding displacement pattern

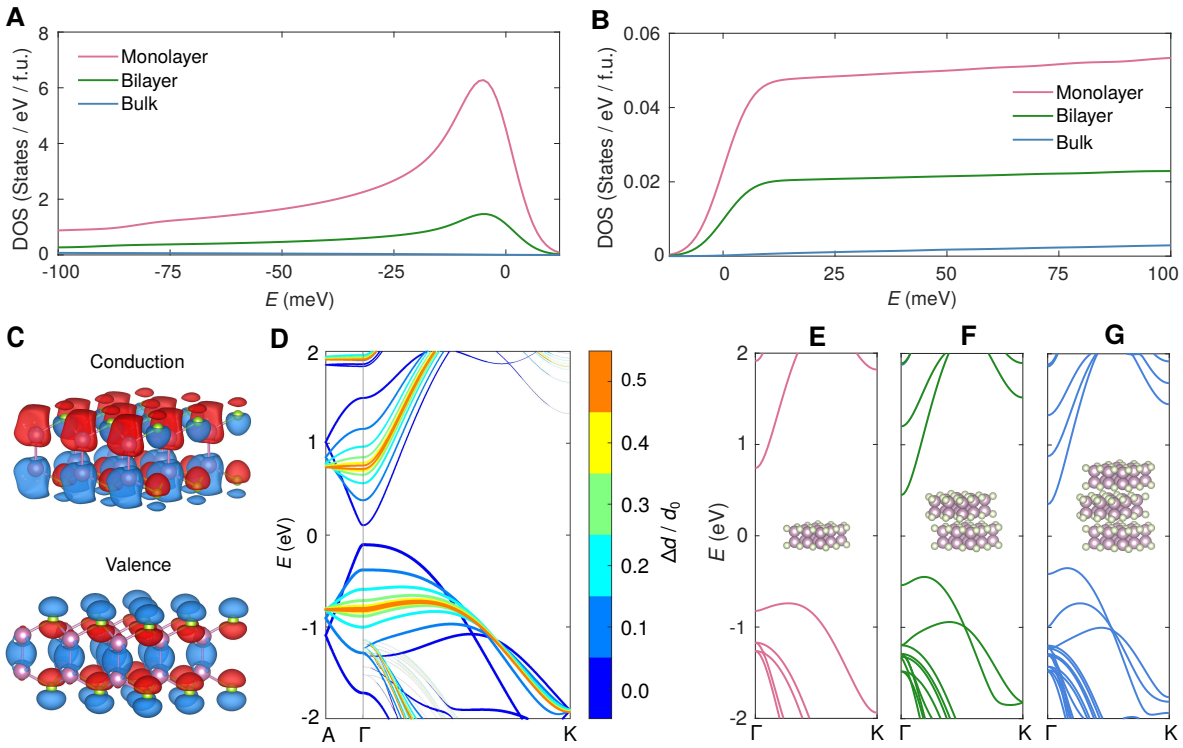

Figure 3: **Interlayer coupling and thickness-dependent electronic density of states.** (**A** and **B**) Calculated valence (left) and conduction (right) band DOS in the vicinity of the band edges, for monolayer, bilayer, and bulk InSe. The energies are referred to the respective band extrema. (**C**) Isosurfaces of the electron wavefunctions at the band edges (Γ-point) for InSe monolayer. (**D**) Sensitivity of the band gap and band edge curvature of bulk InSe to the interlayer separation d. The color-coded bands correspond to calculations where the separation is increased to 150% of the bulk value $d_0 = 8.3$ Å in steps of 10%. Each color represents a different value of the interlayer separation, as given by the relative change with respect to the bulk value, $\Delta d/d_0 = (d - d_0)/d_0$. For clarity we only show the projection of the bands onto p_z states. (**E**–**G**) Emergence of subbands in few-layer InSe along the Γ-K path.

is shown in Supplemental Figure S4F. Yet, despite their different nature, the strength $|g|^2$ of LA-phonon scattering is comparable or even smaller than that of Fröhlich coupling, see Supplementary Figure S6*C*. Taken together, these results indicate that the electron-phonon matrix elements $|g|^2$ are relatively insensitive to the number of layers and to the carrier type. Therefore the strong variations in the carrier mobilities seen in Figure 1*D* and *E* must originate from the last remaining parameter, the density of states (DOS).

Figure 3*A* and *B* shows the DOS of monolayer, bilayer, and bulk InSe in the vicinity

of the band edges. Here we note that the valence band DOS is approximately one order of magnitude higher than the conduction band DOS, and that in both cases the DOS decreases dramatically from monolayer to bulk (see also Supplementary Figure S7 and Supplementary Figure S8). These two observations confirm that the change in $D(E)$ is the dominant mechanism underlying the variation in carrier mobilities in Figure 1. What is the origin of such large variations in the DOS from holes to electrons and from monolayer to bulk?

In the case of hole carriers, the valence band top of monolayer InSe exhibits a Mexican-hat shape (Figure 2E). This band warping gives rise to a 2D van Hove singularity that is visible as a sharp low-energy peak in the DOS. The warping tends to disappear when the InSe layers are stacked as in bulk InSe (Figure 2D), and the DOS decreases accordingly, as can be seen in Figure 3A. A similar sensitivity of the DOS to the interlayer distance is also observed in the case of the conduction band (Figure 3B). Such a sensitivity hints at a possible hidden role of the interlayer coupling in the carrier mobilities. We investigate this aspect in greater detail by focusing on the conduction band edge, since electron carriers exhibit the highest mobilities.

Figure 3C shows representative wavefunctions for states near the conduction band edge. These states derive primarily from In and Se s and p_z orbitals (Supplementary Figure S9 and S10). In multilayer stacks, the p_z orbitals interact with their counterparts from neighbouring layers, leading to significant out-of-plane dispersion of the bands as well as small effective masses ($m_z^*/m_e = 0.025$). In InSe this interaction is particularly strong, in fact the band gap is reduced by nearly 1 eV upon bringing individual monolayers together in the bulk structure (Figure 3D). This is also shown in Figure 3E–G, where we see the emergence of subbands with an energy separation of several hundred meV's when going from monolayer InSe to a trilayer. In order to conceptualize these results we devise a minimal tight-binding model.

We consider a one-orbital, nearest-neighbor tight-binding model as illustrated in Figure 4A. The orbitals of this model are meant to represent the hybrid s/p_z states at the band edges, and occupy the site of a 2D hexagonal lattice with nearest-neighbour hopping matrix

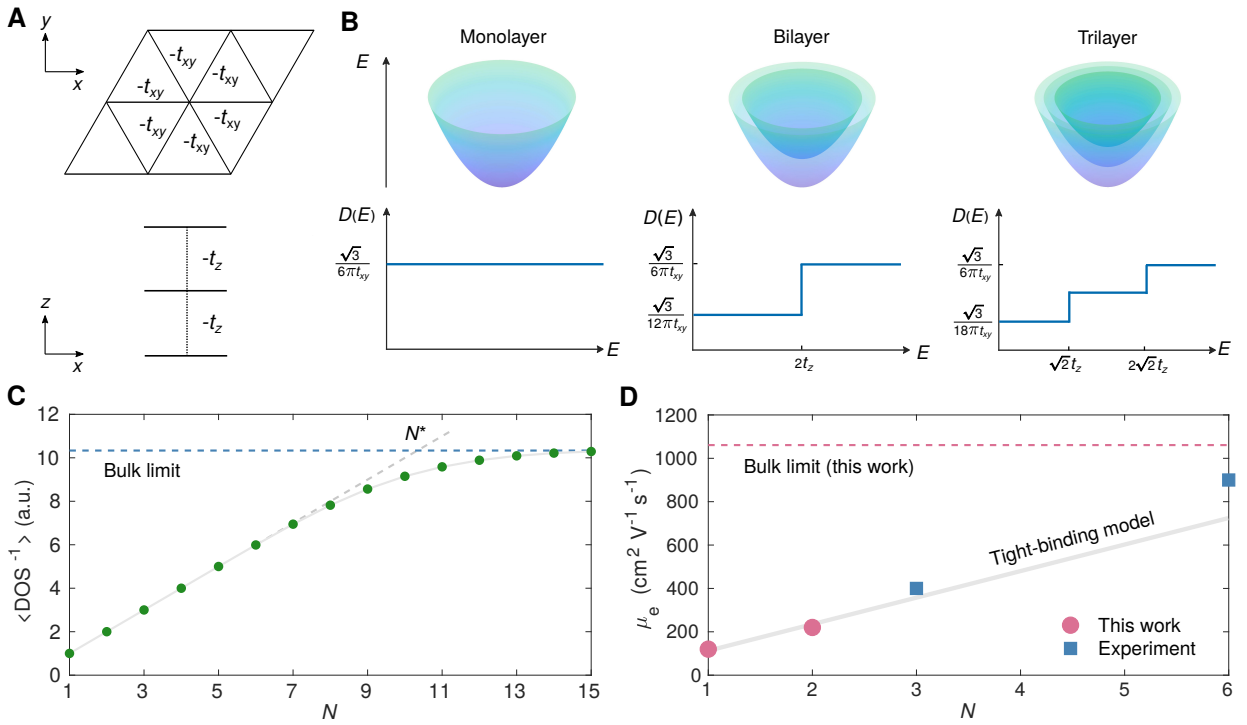

Figure 4: **Dimensional crossover in the mobility of InSe and 2D materials.** (**A**) Schematic of the tight-binding model used to describe the thickness dependence of the DOS of InSe. (**B**) Low-energy electronic band structures and the corresponding DOS per site from the tight-binding model, illustrated for monolayer, bilayer, and trilayer, respectively. (**C**) Inverse DOS as a function of the number of layers N within the tight-binding model. The blue dashed line represents the bulk limit, the gray dashed line is the linear approximation at low N. The intersection between these two lines identifies the 2D to 3D crossover N^*. (**D**) Summary map of the electron mobilities in InSe, including experimental data for three- and six-layer samples,[6] calculations based on the *ab initio* Boltzmann equation, and the tight-binding model.

elements $-t_{xy}$. The 2D layers are then stacked vertically, with interlayer hopping $-t_z$. The band structures of this model are readily obtained, as discussed in Supplementary Note S1. In the monolayer, the DOS per site is $D_1 = \sqrt{3}/6\pi t_{xy}$, independent of energy. When we consider multiple layers, the interlayer hopping leads to the formation of subbands, and the DOS per site exhibits a stepwise decrease towards the band bottom, as shown in Figure 4*B* (see also Supplementary Figure S11 and S12). For a N-layer system the DOS at the band bottom is easily seen to be D_1/N. By combining this result with the Drude model we can expect that the mobility will increase linearly with the number of layers.

In order to place this reasoning on quantitative ground, we calculate explicitly the average reciprocal DOS that enters the calculations of mobilities, $\langle D^{-1} \rangle$, and determine the interlayer hopping by comparing the tight-binding band structure of the bilayer with our *ab initio* calculations ($t_z = 0.38$ eV, Supplementary Figure S13 and Supplementary Note S2). Figure 4*C* shows $\langle D^{-1} \rangle$ as a function of N, calculated at room temperature. We see that this quantity exhibits indeed a linear increase for the few-layer system, but it saturates to a constant value towards the bulk. This behavior is a manifestation of the dimensionality crossover from a 2D system, for which $D(E) = \text{const}$, to its 3D counterpart, for which $D(E) \propto E^{1/2}$. The crossover thickness is controlled by the interlayer hopping t_z, and corresponds to $N^* = 10$ in the case of InSe. Based on this analysis we predict that the electron mobility of InSe will increase almost linearly with the number of layers up to $N \sim 10$, equivalent of thickness $d \sim 8$ nm, and saturate beyond this thickness.

In Figure 4*D* we test the predictions of our simplified model against our brute-force *ab-initio* calculations of mobilities of monolayer, bilayer, and bulk InSe, as well as experimental values for three-layer and six-layer samples.[6] We see that both *ab initio* calculations and experiments nicely agree with our simplified model. The small deviations from linearity are likely due to the simplifying assumptions used in our model, as well as the effect of free carrier and substrate-induced screening in the experimental samples, which is known to enhance carrier mobilities by weakening Fröhlich interactions.[25] Apart from these small corrections, the present analysis unambiguously demonstrates that materials dimensionality plays a central role in the transport properties of InSe.

To the best of our knowledge, the possibility of controlling carrier mobilities in 2D materials via dimensionality, and the existence of a dimensional crossover from 2D to 3D, have never been pointed out before. It is therefore natural to ask whether this novel effect is unique to InSe, or it is a general feature of 2D semiconductors. To answer this question, we perform a systematic investigation of the carrier mobilities as a function of thickness and interlayer hopping using our tight-binding model. Supplementary Figure S14 shows that

dimensionality plays an important role even when the interlayer coupling is as small as a few tens of meV's. Thus, even in systems with weak interlayer coupling, the mobility of multilayers could be several times higher than in the monolayer.

Our findings suggest that the dimensional crossover identified in this work could occur in a wide range of 2D semiconductors, from transition metal dichalcogenides,[26] to phosphorene,[27] and monochalcogenides.[3] Indeed, the key feature that is essential to the conclusions drawn from our model is the formation of subbands with parabolic band edges in multilayer systems. These subbands originate from the interlayer coupling, and lead to a DOS which depends on the number of layers. We checked that this feature is also present in the band-structure evolution of MoS_2 and phosphorene multilayers (see Supplementary Figure S15 and Figure S16). In line with our findings, experimental evidence suggested that the interlayer coupling in phosphorene is comparable to InSe,[27] and the formation of narrowly-spaced subbands was observed theoretically in a broad class of transition metal dichalcogenides.[28] Furthermore, recent experiments reported thickness-dependent carrier mobilities in few-layer MoS_2, but the origin of this effect has remained elusive thus far.[10] Based on our work, we can anticipate that the layer-dependent mobilities in MoS_2 could also originate from a dimensionality effect, although this will certainly warrant a separate investigation.

While our work reveals the crucial role of band-edge DOS in the dimensional crossover of the intrinsic carrier mobility of 2D semiconductors, we emphasize that our model focuses on gapped semiconductors with parabolic band edges and with effective masses weakly-dependent on the number of layers. Hence, our model should not be used for systems like graphene, which is a semimetal with linear band dispersion near the Fermi level. Unlike the gapped 2D semiconductors discussed in the present work, the change from linear to parabolic dispersion from monolayer to bilayer graphene (Supplementary Figure S17) results in the reduction of carrier mobilities.[29,30] Having identified the band-edge DOS as a key driver of the dimensionality crossover in the mobility of 2D materials, it will be interesting to investigate experimentally if the layer-dependent intrinsic carrier mobilities of 2D semiconductors could

all fit into the simple description provided by our model.

In conclusion, we found that materials dimensionality modulates the intrinsic carrier mobility of InSe and other layered materials over an extremely wide range. We demonstrated that this novel, intrinsic effect originates from the evolution of the electronic structure from 2D to 3D with thickness, and that below a critical thickness it is responsible for a linear increase of the electron mobility with the number of atomic layers. By providing a simple conceptual framework to rationalize transport measurements on InSe, our work will serve as a blueprint for the development of 2D electronics based on this new semiconductor. More generally, as quantum-mechanical coupling between the wavefunctions of adjacent layers is ubiquitous in 2D semiconductors and their heterostructures, the dimensionality effect discovered in this work opens intriguing new opportunities for controlling carrier transport at the nanoscale via van der Waals epitaxy.

Methods. *Ground-state calculations. Ab initio* calculations of bulk β-InSe (space group $P6_3/mmc$) were carried out using the experimental lattice parameters $a = 4.005$ Å and $c = 16.660$ Å.[12] We used DFT within the local density gradient approximation of Perdew and Wang.[31] The core-valence interaction was described using Troullier-Martins norm-conserving pseudopotentials,[32] with the semicore In-4*d* states explicitly taken into account. Electronic wavefunctions were expanded in a plane-wave basis set with kinetic energy cutoff of 100 Ry, which is sufficient to converge the total energy within 2 meV per atom. The Brillouin zone was sampled using a $12 \times 12 \times 4$ Monkhorst-Pack mesh shifted along the *c*-axis. The atomic positions were relaxed with a force convergence criterion of 10^{-5} Ry/Bohr. Dielectric and lattice-dynamical properties were calculated using density functional perturbation theory (DFPT). For the calculation of the Fröhlich electron-phonon matrix elements we used the converged dielectric tensors and Born effective charges obtained using a $31 \times 31 \times 31$ Monkhorst-Pack mesh.

Monolayer and bilayer InSe were described using a vacuum-slab model. The in-plane lattice constants were fixed to be the same as those in the bulk. The dimensions of the cells

in the out-of-plane direction were 20 Å and 25 Å for monolayer and bilayer respectively; we checked that this is enough to make interlayer electronic interaction negligible. A slightly higher planewaves cut-off of 120 Ry was used in this case, in order to ensure the convergence of lattice dynamical properties. For the monolayer and bilayer we sampled the Brillouin zone using a $12 \times 12 \times 1$ unshifted Monkhorst-Pack mesh.

The calculated dielectric tensors and Born effective charges of monolayer and bulk InSe are shown in Supplementary Figure S18 and Table S2. All DFT and DFPT calculations were performed using the Quantum ESPRESSO package.[33]

Electron-phonon coupling. Calculations of electron-phonon couplings and carrier mobilities were performed using the EPW code.[34,35] For bulk β-InSe, the electron-phonon matrix elements were initially computed on a $8 \times 8 \times 4$ electronic grid and a $4 \times 4 \times 4$ phonon grid, which were subsequently interpolated onto fine grids with *ab initio* accuracy, using maximally-localised Wannier functions.[36] The Fröhlich electron-phonon matrix elements were calculated using the method of ref.[22] In order to obtain accurate carrier mobilities, we used quasi-random fine grids with Cauchy distributions centered at Γ. The weight of each point in these grids is given by the corresponding Voronoi volume in the Brillouin zone. A finite broadening of 1 meV was used to evaluate the Dirac delta functions in Eq. (2) below. Detailed convergence tests are reported in Supplementary Figure S19.

For monolayer and bilayer, the use of slab model means that these systems are effectively described as three-dimensional InSe/vacuum superlattices. For these systems, the analytic expression for Fröhlich electron-phonon matrix elements of ref.[22] is strictly valid only in the long-wavelength limit ($\mathbf{q} \to 0$). To address this point, before interpolation we computed the electron-phonon matrix elements on a coarse $12 \times 12 \times 2$ $\mathbf{k}$ grid and a $12 \times 12 \times 2$ $\mathbf{q}$ grid. We found that these grids were sufficient to achieve excellent accuracy in the interpolation of electron-phonon matrix-elements over the whole Brillouin zone (as compared to explicit DFPT calculations). For bilayer InSe, due to computational cost, the coarse $\mathbf{q}$ grid was reduced to $6 \times 6 \times 2$. In the case of monolayer InSe this trimming changes the carrier

mobilities by less than five percent, therefore we consider 5% to be our error bar in the mobilities of the bilayer. We also checked that the calculated mobilities are not sensitive to the vacuum size used in the calculations. Complete tests are reported in Supplementary Figure S20.

The carrier concentration for computing the mobilities was set at 10^{13} cm^{-3} for all systems. For monolayer and few-layer systems, when computing volume and carrier concentration, the dimension in the out-of-plane direction is taken to be the bulk interlayer distance multiplied by the number of layers. In our calculations we found that the intrinsic carrier density of InSe does not exceed 10^{13} cm^{-3} up to 500 K, the highest temperature considered in this work. We have also calculated the mobilities for carrier densities ranging from 10^{11} cm^{-3} to 10^{15} cm^{-3}. As shown in the Supplementary Figure S21, the calculated intrinsic carrier mobilities are essentially independent of carrier density within (and below) this range. We note that in our calculations free-carrier screening[37] and electron-plasmon scattering[38] are not included, since these effects are negligible in the limit of intrinsic carrier density.

Spin-orbit coupling and many-body quasiparticle corrections. Previous work pointed out that spin-orbit coupling (SOC) and many-body quasiparticle corrections affect the calculated carrier mobility mainly through the change in the effective mass.[15] To test these effects, in Supplementary Figure S22 we compare the electronic band structures of bulk and monolayer InSe with and without SOC. The effects of SOC on the band structure is found to be small. In particular, SOC does not change the electron effective mass of monolayer, and only slightly reduces the effective masses of bulk InSe. Recent GW calculations of the band structures of InSe indicated that quasi-particle corrections also have a small effect on the in-plane effective masses of InSe.[39] We therefore expect that the calculated carrier mobilities will not change significantly upon including SOC and many-body quasiparticle corrections. This is supported by the good agreement of our calculated effective masses and carrier mobilities with available experimental data.

Carrier scattering rates and mobilities. Carrier mobilities were computed using the *ab*

initio Boltzmann transport equation in the self-energy relaxation time approximation.[15] In this framework, the electron mobility μ_e is given by:

$$\mu_{e,\alpha\beta} = \frac{-e}{n_e \Omega} \sum_{n \in \mathrm{CB}} \int \frac{d\mathbf{k}}{\Omega_{\mathrm{BZ}}} \frac{\partial f_{n\mathbf{k}}}{\partial \varepsilon_{n\mathbf{k}}} v_{n\mathbf{k},\alpha} v_{n\mathbf{k},\beta} \tau_{n\mathbf{k}}, \tag{1}$$

where α and β denote Cartesian coordinates, n_e is the carrier concentration, and Ω denotes the volume of the crystalline unit cell. The summation is over the band index n, and the integral is over the electron wavevectors $\mathbf{k}$ in the first Brillouin zone, whose volume is Ω_{BZ}. $\varepsilon_{n\mathbf{k}}$ and $f_{n\mathbf{k}}$ represent the Kohn-Sham energies and occupation numbers, respectively, and $v_{n\mathbf{k}}$ is the band velocity. The carrier lifetime $\tau_{n\mathbf{k}}$ are computed within the Fan-Migdal approximation:[40]

$$\begin{aligned} \frac{1}{\tau_{n\mathbf{k}}} =& \frac{2\pi}{\hbar} \sum_{m\nu} \int \frac{d\mathbf{q}}{\Omega_{\mathrm{B}Z}} |g_{mn\nu}(\mathbf{k},\mathbf{q})|^2 \\ & \times \left[(1 - f_{m\mathbf{k}+\mathbf{q}} + n_{\mathbf{q}\nu}) \delta(\varepsilon_{n\mathbf{k}} - \varepsilon_{m\mathbf{k}+\mathbf{q}} - \hbar\omega_{\mathbf{q}\nu}) \right. \\ & \left. + (f_{m\mathbf{k}+\mathbf{q}} + n_{\mathbf{q}\nu}) \delta(\varepsilon_{n\mathbf{k}} - \varepsilon_{m\mathbf{k}+\mathbf{q}} + \hbar\omega_{\mathbf{q}\nu}) \right], \end{aligned} \tag{2}$$

where $\mathbf{q}$ is a phonon wavevector, and the summation is over the electron band index m and phonon branch index ν. The phonon energies and the corresponding occupation numbers are denoted by $\hbar\omega_{\mathbf{q}\nu}$ and $n_{\mathbf{q}\nu}$, respectively. The electron-phonon matrix element $g_{mn\nu}(\mathbf{k},\mathbf{q})$ represent the probability amplitude of an electron scattering from a Bloch state $n\mathbf{k}$ to another state labelled by m and $\mathbf{k}+\mathbf{q}$, due to the emission or absorption of a phonon with indices $\mathbf{q}\nu$. The Dirac delta functions reflect the conservation of energy during the scattering process. The above formula is consistent with Fermi's Golden Rule.

As the phonon energy scale is typically much smaller than that of electrons, the above equation indicates that the electron-phonon scattering rate scales with the electron phonon

matrix elements $|g_{mn\nu}(\mathbf{k},\mathbf{q})|^2$ and with the electronic density of states:

$$D(\varepsilon) = \sum_m \int \frac{d\mathbf{k}}{\Omega_{\mathrm{BZ}}} \delta(\varepsilon - \varepsilon_{m\mathbf{k}}). \tag{3}$$

This definition of the DOS yields the number of states per energy per unit cell. In order to compare DOS and matrix elements between monolayer, bilayer, and bulk InSe, we introduce n_{f}, which represents the number of chemical formula units per unit cell. The density of states is then scaled as $D(\varepsilon)/n_{\mathrm{f}}$, and the matrix elements are scaled as $n_{\mathrm{f}}|g_{mn\nu}(\mathbf{k},\mathbf{q})|^2$. This scaling allows us to compare DOS and matrix elements across different number of layers and cell sizes, while leaving unchanged physical observables such as carrier scattering rates and mobilities.

Associated Content

Supporting Information

Supplementary Note S1 and S2; Supplementary Figure S1–S22; Supplementary Table S1 and S2.

Author Information

Corresponding Author

*(F.G.) Email: feliciano.giustino@materials.ox.ac.uk

Acknowledgements

The authors gratefully acknowledge fruitful discussions with C. Verdi and G. Volonakis. This work was supported by the Leverhulme Trust (Grant RL-2012-001), the Graphene Flagship (Horizon 2020 Grant No. 785219 - GrapheneCore2) and the UK Engineering and Physical Sciences Research Council (Grant EP/M020517/1). W. Li and F. Giustino acknowledge support from the European Unions Horizon 2020 research and innovation programme under the

Marie Skłodowska-Curie grant agreement No. 743580. This work used the University of Oxford Advanced Research Computing (ARC) facility (http://dx.doi.org/10.5281/zenodo.22558), the DECI resource Abel based in Oslo, and MareNostrum at BSC-CNS Spain with support from the PRACE AISBL.

References

(1) Novoselov, K. S.; Jiang, D.; Schedin, F.; Booth, T. J.; Khotkevich, V. V.; Morozov, S. V.; Geim, A. K. Two-dimensional atomic crystals. *Proc. Natl. Acad. Sci. U.S.A.* **2005**, *102*, 10451–10453.

(2) Geim, A. K.; Grigorieva, I. V. Van der Waals heterostructures. *Nature* **2013**, *499*, 419–425.

(3) Novoselov, K. S.; Mishchenko, A.; Carvalho, A.; H., C. N. A. 2D materials and van der Waals heterostructures. *Science* **2016**, *353*, aac9439.

(4) Akinwande, D.; Petrone, N.; Hone, J. Two-dimensional flexible nanoelectronics. *Nat. Commun.* **2014**, *5*, 5678.

(5) Chhowalla, M.; Jena, D.; Zhang, H. Two-dimensional semiconductors for transistors. *Nat. Rev. Mater* **2016**, *1*, 16052.

(6) Bandurin, D. A.; Tyurnina, A. V.; Yu, G. L.; Mishchenko, A.; Zólyomi, V.; Morozov, S. V.; Kumar, R. K.; Gorbachev, R. V.; Kudrynskyi, Z. R.; Pezzini, S. et al. High electron mobility, quantum Hall effect and anomalous optical response in atomically thin InSe. *Nat. Nanotechnol.* **2016**, *12*, 223–227.

(7) Feng, W.; Zheng, W.; Cao, W.; Hu, P. Back Gated Multilayer InSe Transistors with Enhanced Carrier Mobilities via the Suppression of Carrier Scattering from a Dielectric Interface. *Adv. Mater.* **2014**, *26*, 6587–6593.

(8) Sucharitakul, S.; Goble, N. J.; Kumar, U. R.; Sankar, R.; Bogorad, A. A.; Chou, F.-C.; Chen, Y.; Gao, X. P. A. Intrinsic electron mobility exceeding 10^3 $cm^2/(V\ s)$ in multilayer InSe FETs. *Nano Lett.* **2015**, *15*, 3815–3819.

(9) Castellanos-Gomez, A. Why all the fuss about 2D semiconductors? *Nat. Photonics* **2016**, *10*, 202–204.

(10) Cui, X.; Lee, G.-H.; Kim, Y. D.; Arefe, G.; Huang, P. Y.; Lee, C.-H.; Chenet, D. A.; Zhang, X.; Wang, L.; Ye, F. et al. Multi-terminal transport measurements of MoS_2 using a van der Waals heterostructure device platform. *Nat. Nanotechnol.* **2015**, *10*, 534–540.

(11) Kim, J. H.; Kim, T. H.; Lee, H.; Park, Y. R.; Choi, W.; Lee, C. J. Thickness-dependent electron mobility of single and few-layer MoS_2 thin-film transistors. *AIP Adv.* **2016**, *6*, 065106.

(12) Politano, A.; Campi, D.; Cattelan, M.; Ben Amara, I.; Jaziri, S.; Mazzotti, A.; Barinov, A.; Gürbulak, B.; Duman, S.; S., A. et al. Indium selenide: an insight into electronic band structure and surface excitations. *Sci. Rep.* **2017**, *7*, 3445.

(13) Rigoult, J.; Rimsky, A.; Kuhn, A. Refinement of the 3R γ-indium monoselenide structure type. *Acta Cryst. B* **1980**, *36*, 916–918.

(14) Carlone, C.; Jandl, S.; Shanks, H. R. Optical phonons and crystalline symmetry of InSe. *Phys. Status Solidi B* **1981**, *103*, 123–130.

(15) Poncé, S.; Margine, E. R.; Giustino, F. Towards predictive many-body calculations of phonon-limited carrier mobilities in semiconductors. *Phys. Rev. B* **2018**, *97*, 121201.

(16) Ashcroft, N. W.; Mermin, N. D. *Introduction to Solid State Physics*; Saunders, Philadelphia, 1976.

(17) Segura, A.; Pomer, F.; Cantarero, A.; Krause, W.; Chevy, A. Electron scattering mechanisms in n-type indium selenide. *Phys. Rev. B* **1984**, *29*, 5708–5717.

(18) Segura, A.; Martinez-Tomás, C.; Casanovas, A.; Cantarero, A.; Martinez-Pastor, J.; Chevy, A. Carrier scattering mechanisms in P-type indium selenide. *Appl. Phys. A* **1989**, *48*, 445–450.

(19) Kress-Rogers, E.; Nicholas, R. J.; Portal, J. C.; Chevy, A. Cyclotron resonance studies on bulk and two-dimensional conduction electrons in InSe. *Solid State Commun.* **1982**, *44*, 379–383.

(20) Grimvall, G. *The electron-phonon interaction in metals*; North-Holland, Amsterdam, 1981.

(21) Sun, C.; Xiang, H.; Xu, B.; Xia, Y.; Yin, J.; Liu, Z. Ab initio study of carrier mobility of few-layer InSe. *Appl. Phys. Express* **2016**, *9*, 035203.

(22) Verdi, C.; Giustino, F. Fröhlich Electron-Phonon Vertex from First Principles. *Phys. Rev. Lett.* **2015**, *115*, 176401.

(23) Zólyomi, V.; Drummond, N. D.; Fal'ko, V. I. Electrons and phonons in single layers of hexagonal indium chalcogenides from ab initio calculations. *Phys. Rev. B* **2014**, *89*, 205416.

(24) Rybkovskiy, D. V.; Osadchy, A. V.; Obraztsova, E. D. Transition from parabolic to ring-shaped valence band maximum in few-layer GaS, GaSe, and InSe. *Phys. Rev. B* **2014**, *90*, 235302.

(25) Ma, N.; Jena, D. Charge scattering and mobility in atomically thin semiconductors. *Phys. Rev. X* **2014**, *4*, 011043.

(26) Manzeli, S.; Ovchinnikov, D.; Pasquier, D.; Yazyev, O. V.; Kis, A. 2D transition metal dichalcogenides. *Nat. Rev. Mater.* **2017**, *2*, 17033.

(27) Li, L.; Kim, J.; Jin, C.; Ye, G. J.; Qiu, D. Y.; da Jornada, F. H.; Shi, Z.; Chen, L.; Zhang, Z.; Yang, F. et al. Direct observation of the layer-dependent electronic structure in phosphorene. *Nat. Nanotechnol.* **2017**, *12*, 21–25.

(28) Kuc, A.; Zibouche, N.; Heine, T. Influence of quantum confinement on the electronic structure of the transition metal sulfide TS_2. *Phys. Rev. B* **2011**, *83*, 245213.

(29) Nagashio, K.; Nishimura, T.; Kita, K.; Toriumi, A. Mobility variations in mono- and multi-layer graphene films. *Appl. Phys. Express* **2009**, *2*, 025003.

(30) Li, X.; Borysenko, K. M.; Nardelli, M. B.; Kim, K. W. Electron transport properties of bilayer graphene. *Phys. Rev. B* **2011**, *84*.

(31) Perdew, J. P.; Wang, Y. Accurate and simple analytic representation of the electron-gas correlation energy. *Phys. Rev. B* **1992**, *45*, 13244–13249.

(32) Troullier, N.; Martins, J. Efficient pseudopotentials for plane-wave calculations. *Phys. Rev. B* **1991**, *43*, 1993–2006.

(33) Giannozzi, P.; Andreussi, O.; Brumme, T.; Bunau, O.; Nardelli, M. B.; Calandra, M.; Car, R.; Cavazzoni, C.; Ceresoli, D.; Cococcioni, M. et al. Advanced capabilities for materials modelling with Quantum ESPRESSO. *Journal of Physics: Condensed Matter* **2017**, *29*, 465901.

(34) Giustino, F.; Cohen, M. L.; Louie, S. G. Electron-phonon interaction using Wannier functions. *Phys. Rev. B* **2007**, *76*, 165108.

(35) Poncé, S.; Margine, E. R.; Verdi, C.; Giustino, F. EPW: Electron–phonon coupling, transport and superconducting properties using maximally localized Wannier functions. *Comput. Phys. Commun.* **2016**, *209*, 116–133.

(36) Mostofi, A. A.; Y., J. R.; Pizzi, G.; Lee, Y.-S.; Souza, I.; Vanderbilt, D.; Marzari, N.

An updated version of wannier90: A tool for obtaining maximally-localised Wannier functions. *Comput. Phys. Commun.* **2014**, *185*, 2309–2310.

(37) Verdi, C.; Caruso, F.; Giustino, F. Origin of the crossover from polarons to Fermi liquids in transition metal oxides. *Nat. Commun.* **2017**, *8*, 15769.

(38) Caruso, F.; Giustino, F. Theory of electron-plasmon coupling in semiconductors. *Phys. Rev. B* **2016**, *94*, 115208.

(39) Li, Y.; Wang, T.; Wu, M.; Cao, T.; Chen, Y.; Shankar, R.; Ulaganathan, R. K.; Chou, F.; Wetzel, C.; Xu, C.-Y. et al. Ultrasensitive tunability of the direct bandgap of 2D InSe flakes via strain engineering. *2D Mater.* **2018**, *5*, 021002.

(40) Giustino, F. Electron-phonon interactions from first principles. *Rev. Mod. Phys.* **2017**, *89*, 015003.